ACS OMEGA

http://pubs.acs.org/journal/acsodf

Article

Nuclear Magnetic Resonance Dipolar Cross-Relaxation Interaction between Nanoconfined Fluids and Matrix Solids

Jin-Hong Chen,* Chao Liu, Stacey M Althaus, and Mohammed Boudjatit

Cite This: *ACS Omega* 2022, 7, 45189−45196

Read Online

ACCESS | Metrics & More | Article Recommendations | Supporting Information

ABSTRACT: Many different methods have been developed to investigate fluid−solid interactions in nanoporous systems. These methods either only work in the liquid phase or provide an indirect measurement by probing the fluid−solid interaction based on a measured property change of the fluid or solid under different sample conditions. Here, we report a direct measurement technique using NMR dipolar cross-relaxation between the nanoconfined fluids and the matrix solids. The method was tested using a methyl-functionalized mesostructured silica saturated with methanol as a model sample. A formal theory was established to describe the enhanced dipolar cross-relaxation interaction between the nanoconfined fluids and the matrix solids. Both the experiment and theory showed that nanoconfinement of the fluids enhances the dipolar cross-relaxation interaction between the fluid and the matrix solids, which can be applied to investigate the fluid−solid interaction for various materials of a similar nanostructure.

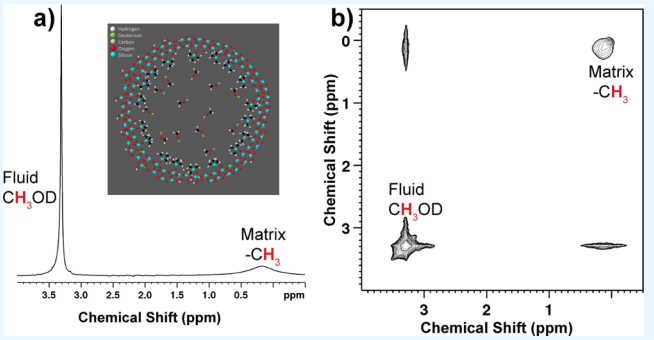

INTRODUCTION

Fluid−solid interactions are ubiquitous in natural and manmade porous materials. The interfacial interaction between a fluid and a solid significantly influences the properties of the solid as well as the storage and transport of the fluid.[1−3] This interaction is of special importance in nanoporous materials because of the large interfacial areas and high surface-to-volume ratios.[4] Methods to quantify the fluid−solid interaction thus have broad applications in many different nanomaterials including synthesized mesoporous silica nanoparticles, carbon nanotubes, metal−organic frameworks, and natural nanomaterials, such as zeolites, shale, etc. Moreover, materials with significant fluid−solid interactions have major economic impacts on hydrocarbon extraction,[5] energy storage,[6] and radioactive waste disposal.[7] In shales and coalbeds, the capacity for natural gas extraction[8,9] and greenhouse gas sequestration[10] is determined by the gas adsorption and transportation through the nanopores embedded in their matrixes. Thus, there is a great need to understand and quantify the interfacial interaction in many of these nanoporous materials.

Many different methods have been developed to investigate the fluid−solid interaction, such as isothermal titration calorimetry (ITC),[11,12] surface adsorption,[13,14] neutron or X-ray scattering,[15,16] and zeta potential analysis.[17] ITC is a very useful measurement of the thermodynamic parameters of interactions, but the method only works in solution. Most other measurement methods are indirect and probe the fluid−solid interaction based on the measured property change of the fluid or solid under different sample conditions. Analytical and computational methods are also widely used to study the fluid−solid interaction.[18]

Nuclear magnetic resonance (NMR) can directly measure the fluid−solid interfacial interaction using the information from nuclear spin dipolar coupling. Dipolar coupling of nuclear spins is particularly important in magnetic resonance spectroscopy and imaging because it depends on distance, orientation, and dynamics.[19] The net dipolar coupling in solid-state NMR experiments provides a direct approach to extract information about structures and dynamics[19] and has been used to study interaction of fluid molecules on the solid surface.[20,21] Dipolar coupling in isotropic fluids averages to zero as a result of molecular Brownian diffusion and becomes a key relaxation mechanism.[22] The dipolar cross-relaxation, also called the nuclear Overhauser effect (NOE), has been the most important and extensively used NMR method in determining structure with molecular dynamics, especially for macromolecules such as proteins and nucleic acids.[23] NMR has also been widely applied to study porous materials, mainly by measuring nuclear spin−lattice (longitudinal) relaxation time T_1[24,25] and/or spin−spin (transverse) relaxation time

Received: August 31, 2022
Accepted: November 15, 2022
Published: December 2, 2022

ACS Publications

© 2022 The Authors. Published by American Chemical Society

https://doi.org/10.1021/acsomega.2c05639
ACS Omega 2022, 7, 45189−45196

T_2.[26,27] T_1 and T_2 have also been extensively used to study porosity, pore size distribution, and fluid saturation for subsurface rock samples.[28] However, the T_1 and T_2 of pore fluids depend on multiple interactions including intramolecular and intermolecular dipolar coupling of the fluid spins, coupling of fluid spins with solid spins of the pore surface and/or matrix, and interaction of fluid spins with the paramagnetic electron spins on the pore surface.[29] Therefore, it can be challenging from the measured T_1 and T_2 to isolate the fluid−solid relaxation, which can provide information on the intermolecular interaction between the fluid and matrix solid in porous materials.

Here, we investigate the direct measurement of dipolar cross-relaxation of nanoconfined fluids with the matrix solids using a methyl functionalized mesostructured silica (MCM41-C1) saturated with methanol as a model sample. Experimentally, we used solid-state NMR with magic-angle-spinning (MAS)[30] to suppress line broadening from local susceptibility heterogeneity.[31] This resulted in narrow peaks of the methyl proton resonances and allowed easy measurement of the cross-relaxation rate between the nanoconfined fluid with the matrix solids. The drastically different behaviors between materials at the nano scale and ones at the bulk scale are well documented and can be related to the boundary conditions at nanometer or bulk scales.[4] We have observed that intermolecular cross-relaxation in nanofluidics were enhanced by two orders of magnitude as a result of nanoconfinement on the molecular translational diffusion.[32] Here, we further show how nanoconfinement of the fluids enhances the dipolar cross-relaxation between the fluid and the matrix solids. The enhanced cross-relaxation of nanoconfined fluid with the matrix solids in this study provides a direct approach to quantify the interaction between them, which can be applied to various materials with a similar nanostructure, such as energy harvest[33] and subsurface extraction from organic-rich shales,[8] nanomedicine,[34,35] membrane science,[36] nanopore DNA sequencing,[37] macromolecules with nano-cavities,[38] and cell organelles containing nanostructures, such as mitochondrial compartments.[39,40]

METHODS

Sample Preparation. Methyl-functionalized MCM-41 (MCM41-C1) was purchased from Glantreo Ltd. (see Figures S1 and S2 in the Supporting Information (SI) for more details). Methanol alcohol-OD (CH_3OD, 98% atoms D, density ρ = 0.813 g/mL, molecular weight = 33.05) was purchased from Sigma Aldrich.

The average pore diameter of MCM41-C1 was determined to be 2.57 nm using N_2 adsorption on a Micromeritics ASAP 2460 instrument and using the BJH desorption data.[41] Figure S2 in the SI shows the pore size distribution of the sample measured using this method.

All the materials were used without further purification. MCM41-C1 was dried under vacuum at 50 °C for 1 week. It was then transferred to a saturation chamber as illustrated in Figure S3 in the SI. Saturation of the nanopores in MCM41-C1 was done based on capillary condensation.[42,43] Specifically, a thin layer of MCM41-C1 was placed in a glass Petri dish, and a separate vial of CH_3OD was placed in a glass desiccator connected to a vacuum pump. We first vacuumed the desiccator to approximately 4800 Pa. We then closed the connection to vacuum and allowed the vapor pressure from methanol to build in the desiccator. The CH_3OD vapor condensed in the nanopores via capillary condensation. This method allows all the nanopores to saturate while leaving no observable fluids between the particles. We then packed the saturated sample into a 4 mm magic-angle-spinning (MAS) NMR rotor from Bruker Biospin Inc. for NMR measurement.

NMR Measurement. All the experiments were done on a Bruker Aeon 500 MHz NMR spectrometer using a 4 mm MAS probe. All the experiments were done at 22 °C unless specifically stated. All the data were acquired at a MAS rate of 8000 Hz. MAS of the sample removes the line-broadening from dipolar coupling[30,44] and from susceptibility inhomogeneity,[45] thereby narrowing the peaks. The former is mainly for the solid components and later for the liquid in the pore. For all the samples, the longitudinal relaxation times (T_1) of all the resonances were estimated using an inversion recovery method[46] to ensure that the interscan delay is greater than five times T_1 for all quantitative experiments.

The 2D nuclear Overhauser effect spectroscopy (NOESY)[47,48] spectra were acquired using a mixing time (τ_m) of 800 ms in the NOESY pulse sequence. The acquired data were 512 and 2048 in the t_1 and t_2 dimensions, respectively. The increments were the same for both t_1 and t_2 dimensions, 333.2 μs. Eight scans were accumulated for each t_1 increment. Sixteen dummy scans were used at the beginning of the pulse sequence.

The selective NOE spectra were acquired using the pulse sequence shown in Figure S4 in the SI. The selective pulse used was a 5 ms E-BURP-2[49] and was on-resonance of the methanol methyl proton. The 5 ms selective pulse decayed the methyl magnetization to 98% of its equilibrium value. At the beginning of the pulse sequence, the combination of the selective 90° pulse and the hard 90° pulse placed the methanol proton magnetization along the z direction while the matrix methyl (C1) magnetization was in the horizontal plane. During the mixing time, z magnetization was transferred from the methanol signal to the C1 signal by the cross-relaxation. The last 90° pulse converts the z magnetization to the horizontal direction for detection. The selective excitation coupled with the eight-step phase cycling suppressed all the initial polarization of the C1 proton magnetization. The entirety of the detected signal from the C1 protons was transferred from the methanol protons through NOE. The NMR signal intensities in a selective-NOE experiment are provided in Figure S4 in the SI.

RESULTS AND DISCUSSION

Nanoconfinement Enhances the Interaction of Confined Fluids with a Nanocavity Matrix. We used a simple system of methyl-functionalized MCM41[50] saturated with deuterated methanol (CH_3OD) to demonstrate the NMR cross-relaxation between the nanoconfined fluids and the pore matrix. MCM41-C1 has an average pore diameter 2.57 nm, measured using nitrogen desorption and the BJH model,[41] as shown in Figure S2 of the SI. This size was selected for practical reasons: the peak intensity of MCM41-C1 is comparable to the peak of the confined liquid in the nanopores in the acquired NMR spectrum at this size.

The 1D proton MAS NMR spectrum of the CH_3OD saturated MCM41-C1 is shown in Figure 1a. A schematic model of CH_3OD in a single MCM41-C1 pore is shown as the inset in Figure 1a where the nucleus of interest, ^1H, is represented with white spheres. Note that in MCM41-C1 the silica matrix is proton-free with the only protons appearing on the surface via alcohol or methyl functional groups. The peak

https://doi.org/10.1021/acsomega.2c05639
ACS Omega 2022, 7, 45189−45196

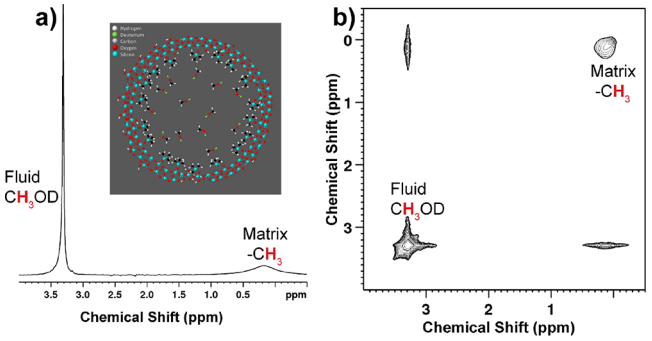

Figure 1. NMR spectra of CH_3OD in methyl-functionalized MCM41 (MCM41-C1). (a) 1D MAS NMR spectrum with an inset showing a schematic model of CH_3OD in MCM41-C1 with a diameter of 2.57 nm. The two peaks at 3.31 and 0.18 ppm are the methyl protons of methanol and MCM41-C1, respectively. (b) 2D phase-sensitive NOESY spectrum with a mixing time 0.8 s.

at 3.31 ppm is the methyl proton of CH_3OD in the pore and the peak at 0.18 ppm is from the methyl proton on the MCM41-C1 pore surface. The linewidths at half height of the two peaks are 11 and 230 Hz, respectively. With MAS suppressing the net dipolar coupling of the solid protons and the magnetic field heterogeneity from local susceptibility for fluid protons,[31] the peak linewidth is now determined by the transverse relaxation T_2. CH_3OD in the pore has a narrow linewidth because the molecular rotational motion is free. The translational motion of CH_3OD is also free in the time scale of $t \sim R^2/4D$, where R is the pore radius and D is the diffusion coefficient of CH_3OD. In contrast, the methyl protons on the MCM41-C1 surface are broader in linewidth due to the solid nature of the matrix, albeit they have some degree of free rotation along the carbon-silicon bond. Without MAS, the methyl proton of MCM41-C1 would be too broad to be detected.

NOESY is a fundamental NMR experiment for measuring cross-relaxation rates used in the determination of molecular structure.[23,47,48] Figure 1b is the phase-sensitive 2D NOESY spectrum[47,48] of the CH_3OD saturated MCM41-C1 at 22 °C. The cross peaks represent the fraction of magnetization transfer from one spin to the other and thus depends on the cross-relaxation rate and sign. In the 2D NOESY spectrum of Figure 1b, the cross peaks between CH_3OD and MCM41-C1 are positive, which is the opposite result that would be generally observed in a bulk solution where the cross peaks are negative from positive intermolecular cross-relaxation rates.[48] In addition, the cross peaks in Figure 1b are strong in comparison to the diagonal peaks, in contrast to the generally weak cross peaks of intermolecular NOEs in bulk fluids with fast molecular tumbling.[32,48]

We used a selective NOE experiment[51,52] to measure the intermolecular cross-relaxation rates between the methanol proton and solid methyl proton for higher accuracy than the 2D method. The pulse sequence with a detailed description of the NMR signals acquired in the selective NOE experiment is shown in Figure S4 in the SI. The signal intensity follows eqs S12 and S13 for the selectively excited spin (fluid methyl protons, spin B) and the non-excited spin (surface solid methyl protons, spin A), respectively. We plotted the best fit to the experimental data at 22 °C in Figure 2a. We fit the two curves simultaneously with common parameters using a nonlinear regression method[53] and obtained the intermolecular cross-relaxation rate $R_{BA} = -0.10 \pm 0.04\ s^{-1}$.

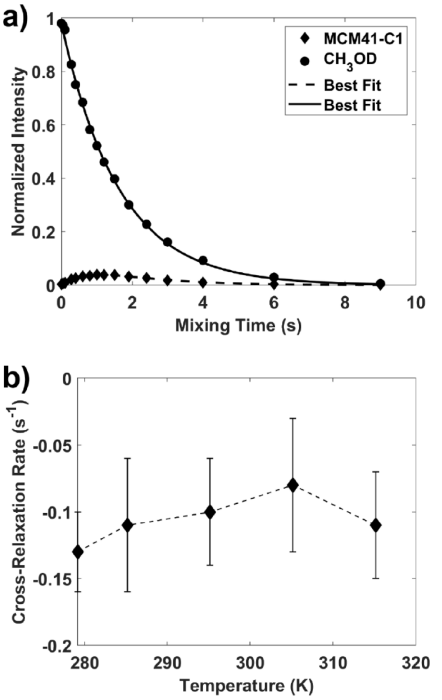

Figure 2. NMR measurement of intermolecular cross-relaxation rate. (a) Signal intensities at different mixing times from the selective-NOE experiments for the CH_3OD proton (triangles) and the MCM41-C1 proton (diamonds) with the best fit (curves) for the two-spin systems. The experiments were done at 22 °C. (b) Measured cross-relaxation rates at different temperatures.

We repeated the selective NOE measurements at four other temperatures and plotted the cross-relaxation rate according to the temperature in Figure 2b. We found that the variation of the cross-relaxation rate over the temperature range is insignificant. The experimental setup does not allow for experimental temperatures below 6 °C. We stopped at 42 °C for concern that the increased vapor pressure in the rotor at higher temperature may loosen the MAS rotor cap.

Nanoconfined Fluid Molecule Diffusion in a Matrix Solid. Nuclear spin relaxation is the result of a fluctuating local magnetic field on one nuclear spin by the neighboring nuclear spins.[22] For a spin pair on two different molecules, the relaxation is caused by the fluctuating intermolecular dipolar coupling due to the translational diffusion.[54,55] Here first, we show simulated results of a fluid molecule confined in nanopores using the random walk method to illustrate that nanoconfinement can modulate the interaction of the fluid spin and the solid spin on the matrix.

Without losing the generality and ease of comparison to experimental results, we only consider a two-dimensional (2D) pore with the assumption that the third dimension is infinitely long. When confined in a pore, a fluid molecule is reflected back into the pore cavity when it encounters the solid pore matrix. Figure 3 shows the simulated molecular diffusion of a fluid particle in two 2D circular pores of different radii: (a) 1.5 nm and (b) 50 nm. In Figure 3b, only a small section of the pore is shown. The red dot represents a fixed spin on the solid pore wall and the black dot represents the initial position of the fluid spin, which is 0.3 nm from the fixed red spin. In the

https://doi.org/10.1021/acsomega.2c05639
ACS Omega 2022, 7, 45189−45196

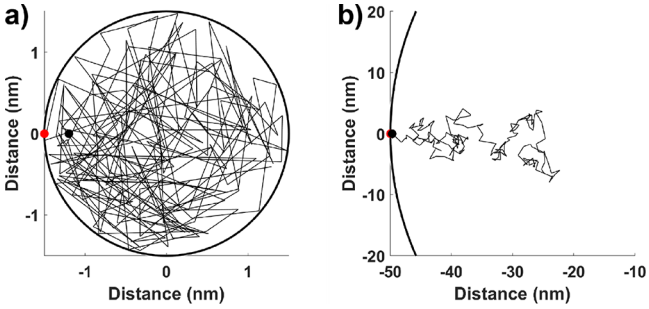

Figure 3. Relative position of two spins from different molecules with one fixed on the pore surface (red dot) and the second one (black dot representing initial position) diffuses in a circular pore with radii of 1.5 nm (a) and 50 nm (b). The black line segments represent 200 step traces of diffusion that started at the same initial positions of 0.3 nm apart. The x and y components of each step were drawn from a normal distribution with a standard deviation of 0.9 nm, corresponding to a time step of 9 ps for a molecule with a diffusion coefficient $D = 2 \times 10^{-9}$ m^2/s based on the 2D Einstein–Smoluchowski relationship: $t = L^2 / 4D$.

simulation, we used a diffusion coefficient of $D = 2 \times 10^{-9}$ m^2/s for the fluid molecule. The solid straight lines represent 200 steps of a random-walk by diffusion of the fluid molecule within the pore. The diffusion process is random and thus Figure 3a and Figure 3b each represent only one scenario among infinite possibilities. It is evident, however, that the spin of a randomly diffusing molecule in a large pore, as illustrated in Figure 3b, has a very small probability of being within 0.5 nm of the fixed red-spin again, as would be required for direct NMR dipolar relaxation. In contrast, the molecule in the smaller pore, which cannot escape the solid boundary, has a much greater probability of being less than 0.5 nm from the solid spin, as illustrated in Figure 3a. As a result, the correlation of dipolar coupling between the fluid and solid spins is enhanced by the nanoconfinement.

Formal Calculation of Nuclear Spin Dipolar Cross-Relaxation of Nanofluidics with a Matrix. In the bulk state, the intermolecular dipolar cross-relaxation rate is positive and small from the well-established method.[48,56] For a proton pair on two free diffusing molecules A and B, the rates are

$$R_{AB} = \frac{\mu_0^2 \gamma_H^4 \hbar^2}{240\pi} \frac{N_A}{D_{AB}\sigma}; \quad R_{BA} = \frac{\mu_0^2 \gamma_H^4 \hbar^2}{240\pi} \frac{N_B}{D_{AB}\sigma} \tag{1}$$

where $\mu_0 = 4\pi \times 10^{-7}$ N/A^2 is the magnetic permeability in vacuum; $\gamma_H = 2.675 \times 10^8$ rad·s^{-1}·T^{-1} is the proton gyromagnetic ratio; $\hbar = 1.05 \times 10^{-34}$ J·s is Plank's constant; N_A and N_B are the number density of the two spins, respectively; σ is the average closest internuclear distance; and D_{AB} is the summation of the diffusion coefficients of the two molecules.[56] Note that σ can be smaller than the summation of the radius of the two molecules because the proton can be on the periphery of the molecules. Equation 1 always gives a positive intermolecular cross-relaxation rates on the magnitude of 10^{-3} s^{-1} in typical bulk solutions. The intermolecular cross-relaxation between a mobile spin and a fixed spin in the bulk state can still be described by eq 1 except that the diffusion coefficient now is only dependent on the mobile spin. Therefore, the cross-relaxation rate in this case would remain positive and have a magnitude of 10^{-3} s^{-1}.

Now, we calculate the dipolar cross-relaxation between nanoconfined fluid and the matrix solid. The cross-relaxation rate for a pair of dipolar coupled spins takes the form[54]

$$R_{cr} = \left(\frac{\mu_o}{4\pi}\right)^2 \hbar^2 \gamma^4 [6J^{(2)}(2\omega_0) - J^{(0)}(0)] \tag{2}$$

where ω_0 is the resonance frequency and is 500.18 MHz, $J^{(k)}(\omega_0)$ $(k = 0, 2)$ are the power spectral densities

$$J^{(k)}(\omega_o) = 2\int_0^{+\infty} G^{(k)}(t)\cos(\omega_o t)dt \tag{3}$$

and $G^{(k)}(t)$ is the correlation function

$$G^{(k)}(t) = c^{(k)} \int\int P(\boldsymbol{r}, \boldsymbol{r}_0, t) F_2^{(k)}(\boldsymbol{r}) F_2^{(k)*}(\boldsymbol{r}_0) N \mathrm{d}^3 r_0 \mathrm{d}^3 r \tag{4}$$

where $c^{(0)} = \frac{48\pi}{15}$, $c^{(1)} = \frac{8\pi}{15}$, $c^{(2)} = \frac{32\pi}{15}$, N is the number density of spins, r is the distance between the two spins, $P(\boldsymbol{r}, \boldsymbol{r}_0, t)\mathrm{d}^3 r$ is the probability that one spin lies within the volume element $\mathrm{d}^3 r$ located at $\boldsymbol{r}$ relative to the other spin at time t, $\boldsymbol{r}_0$ is the initial relative position vector between the two spins at $t = 0$, and $F_2^{(k)}(\boldsymbol{r})$ is a random function of space with $F_2^{(-k)}(\boldsymbol{r}) = F_2^{(k)}(\boldsymbol{r})$*and defined by $F_2^{(k)} = \frac{Y_2^{(k)}(\Omega)}{r^3}$ with $Y_2^{(k)}(\Omega)$ the spherical harmonics. For the 2D circular domain studied here, following the treatment of Faux et al.,[57] the spherical harmonics are functions of the azimuthal angle θ only and $Y_2^{(0)}(\theta) = -\sqrt{5/16\pi}$, $Y_2^{(\pm 2)}(\theta) = \sqrt{15/32\pi}\, e^{\pm 2i\theta}$. A simplification was made by ignoring the contribution of diffusion along the cylindric axis to the overall cross-relaxation. This is a reasonable assumption because diffusion in this direction is in an infinite space, and according to eq 1, the resulting intermolecular cross-relaxation rate is on the order of 10^{-3} s, which accounts for about 1% of the measured rate with nanoconfinement.

To obtain the cross-relaxation rate, one must first obtain the probability function $P(\boldsymbol{r}, \boldsymbol{r}_0, t)$, which is defined by the relative diffusion of the two interacting spins, as illustrated in Figure 3a. Here, we consider schematically in Figure 4a that one spin, O_1', is fixed on the pore surface and the other, O_2', is diffusing within the pore space. Note that spin, O_1', can be at any place on the pore surface. Therefore, both the direction and magnitude of the vector $\overrightarrow{O_1'O_2'}$ change with the movement of the spin O_2'. Note that the closest interspin distance is σ. The longest distance between the two spins is $2R$ when $O_1'O_2'$ is equal to the diameter of the circle shown in Figure 4a. We can

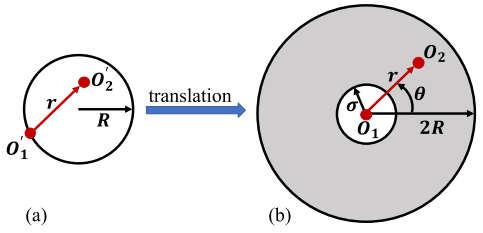

Figure 4. Schematics for (a) the 2D circular domain in which one spin, O_1', is fixed on the solid surface and the other one, O_2', is diffusing inside the circular 2D pore. (b) After the translation of the vector $\overrightarrow{O_1'O_2'}$ to $\overrightarrow{O_1O_2}$, spin, O_1', is fixed at the domain center and spin, O_2', diffuses in the 2D light gray ring area.

https://doi.org/10.1021/acsomega.2c05639
ACS Omega 2022, 7, 45189−45196

apply the translation of the vector $\overrightarrow{O_1'O_2'}$ to $\overrightarrow{O_1O_2}$ where the point O_1 is fixed, as illustrated in Figure 4b. As a result, the movements of O_1' and O_2' are equal to the movement of O_2, which is restricted in a ring area shown in Figure 4b. The inner and outer radii of the ring are σ and $2R$, respectively. Note that the translation does not change the form of probability function $P(\boldsymbol{r}, \boldsymbol{r}_0, t)$ but significantly simplifies the boundary condition.

The probability function $P(\boldsymbol{r}, \boldsymbol{r}_0, t)$ is governed by the following diffusion equation in a two-dimensional circular domain

$$\frac{\partial P(\boldsymbol{r}, \boldsymbol{r}_0, t)}{\partial t} = D\nabla^2 P(\boldsymbol{r}, \boldsymbol{r}_0, t) \tag{5}$$

where $\boldsymbol{r}$ stands for the vector $\overrightarrow{O_1O_2}$ with magnitude of r and azimuth θ, $\boldsymbol{r}_0$ is the initial state of the two spins, $\nabla^2 = \frac{\partial^2}{\partial r^2} + \frac{1}{r}\frac{\partial}{\partial r} + \frac{1}{r^2}\frac{\partial^2}{\partial \theta^2}$, and D is the mutual translational self-diffusion constant between the two spins and thus equal to the diffusion coefficient of the fluid.

The initial and boundary conditions for eq 5 take the following forms

$$P(\boldsymbol{r}, \boldsymbol{r}_0, t = 0) = \delta(r - r_0)\delta(\theta - \theta_0) \tag{6}$$

$$\left.\frac{\partial P(\boldsymbol{r}, \boldsymbol{r}_0, t)}{\partial r}\right|_{r=\sigma} = \left.\frac{\partial P(\boldsymbol{r}, \boldsymbol{r}_0, t)}{\partial r}\right|_{r=2R} = 0 \tag{7}$$

where δ is the Dirac delta. Equation 7 indicates that a fluid molecule is reflected back when it encounters the boundary.

Following Ölçer and Sunderland,[58] the solution of eq 5 with initial condition eq 6 and boundary conditions eq 7 is

$$P(\boldsymbol{r}, \boldsymbol{r}_0, t) = \frac{1}{\pi(4R^2 - \sigma^2)} + \sum_{m=0}^{\infty}\sum_{n=1}^{\infty} \frac{U_m\left(\beta_{mn}\frac{r}{2R}\right)U_m\left(\beta_{mn}\frac{r_0}{2R}\right)}{\pi V_{mn}(1 + \delta_{0m})}\cos m(\theta - \theta_0)\mathrm{e}^{-\beta_{mn}^2 t/\tau} \tag{8}$$

where $\tau = 4R^2/D$ is a characteristic time constant ($\tau \sim 5.57$ ns with $R = 1.5$ nm and $D = 1.21 \times 10^{-9}$ m^2/s) and

$$U_m\left(\beta_{mn}\frac{r}{2R}\right) = J_m'\left(\beta_{mn}\frac{\sigma}{2R}\right)Y_m\left(\beta_{mn}\frac{r}{2R}\right) - Y_m'\left(\beta_{mn}\frac{\sigma}{2R}\right)J_m\left(\beta_{mn}\frac{r}{2R}\right) \tag{9}$$

and

$$V_{mn} = \int_a^b U_m^2\left(\beta_{mn}\frac{r}{2R}\right)r\mathrm{d}r \tag{10}$$

δ_{0m} is the Kronecker delta, $J_n(x)$ and $Y_n(x)$ are the nth order Bessel functions of the first kind and second kind, respectively, and β_{mn} is the nth non-negative root of the following equation

$$J_m'\left(\beta_{mn}\frac{\sigma}{2R}\right)Y_m'(\beta_{mn}) - Y_m'\left(\beta_{mn}\frac{\sigma}{2R}\right)J_m'(\beta_{mn}) = 0 \tag{11}$$

Completing the integration in eq 10, we have

$$V_{mn} = \frac{1}{2}\left(4R^2 - \frac{4m^2R^2}{\beta_{mn}^2}\right)U_m^2(\beta_{mn}) - \frac{8R^2}{\pi^2\beta_{mn}^2}\left(1 - \frac{4m^2R^2}{\beta_{mn}^2\sigma^2}\right) \tag{12}$$

For a 2D circular domain $\mathrm{d}\Omega_0 = r_0\mathrm{d}r_0\mathrm{d}\theta_0$ and $\mathrm{d}\Omega = r\mathrm{d}r\mathrm{d}\theta$, the correlation function eq 4 can be written as

$$G^{(0)}(t) = N\int_\sigma^{2R}\int_0^{2\pi}\int_\sigma^{2R}\int_0^{2\pi}\frac{P(\boldsymbol{r}, \boldsymbol{r}_0, t)}{r^2r_0^2}\mathrm{d}r_0\mathrm{d}\theta_0\mathrm{d}r\mathrm{d}\theta \tag{13}$$

$$G^{(2)}(t) = N\int_\sigma^{2R}\int_0^{2\pi}\int_\sigma^{2R}\int_0^{2\pi}\frac{P(\boldsymbol{r}, \boldsymbol{r}_0, t)}{r^2r_0^2}\mathrm{e}^{2i\theta}\mathrm{e}^{-2i\theta_0}\mathrm{d}r_0\mathrm{d}\theta_0\mathrm{d}r\mathrm{d}\theta \tag{14}$$

Substitution of eq 8 into eqs 13 and 14 gives

$$G^{(0)}(t) = 2\pi N\sum_{n=1}^{\infty}\frac{C_n^2\mathrm{e}^{-\beta_{0n}^2 t/\tau}}{V_{0n}} \tag{15}$$

$$G^{(2)}(t) = 2\pi N\sum_{n=1}^{\infty}\frac{C_n^2\mathrm{e}^{-\beta_{2n}^2 t/\tau}}{V_{2n}} \tag{16}$$

where

$$C_n = \int_\sigma^{2R}\frac{U_0\left(\beta_{0n}\frac{r}{2R}\right)}{r^2}\mathrm{d}r \tag{17}$$

$$D_n = \int_\sigma^{2R}\frac{U_2\left(\beta_{2n}\frac{r}{2R}\right)}{r^2}\mathrm{d}r \tag{18}$$

Using eq 9, we can complete the integration in eqs 17 and 18

$$\begin{aligned} C_n = {} & \frac{1}{2R}J_o'\left(\beta_{0n}\frac{\sigma}{2R}\right)\Big[-Y_0(\beta_{0n})_1F_2\left(1; -\frac{1}{2}, \frac{1}{2}; -\frac{\beta_{0n}^2}{4}\right) + \beta_{0n}Y_1(\beta_{0n})_1F_2\left(1; \frac{1}{2}, \frac{1}{2}; -\frac{\beta_{0n}^2}{4}\right) + \frac{2R}{\sigma}Y_0\left(\beta_{0n}\frac{\sigma}{2R}\right)_1 \\ & F_2\left(1; -\frac{1}{2}, \frac{1}{2}; -\frac{\beta_{0n}^2}{4}\frac{\sigma^2}{4R^2}\right) - \beta_{0n}Y_1\left(\beta_{0n}\frac{\sigma}{2R}\right)_1 \\ & F_2\left(1; \frac{1}{2}, \frac{1}{2}; -\frac{\beta_{0n}^2}{4}\frac{\sigma^2}{4R^2}\right)\Big] - \frac{1}{\sigma}Y_0'\left(\beta_{0n}\frac{\sigma}{2R}\right)_1 \\ & F_2\left(-\frac{1}{2}; \frac{1}{2}, 1; -\frac{\beta_{0n}^2}{4}\frac{\sigma^2}{4R^2}\right) - \frac{1}{2R}Y_0'\left(\beta_{0n}\frac{\sigma}{2R}\right)_1 \\ & F_2\left(-\frac{1}{2}; \frac{1}{2}, 1; -\frac{\beta_{0n}^2}{4}\right) \end{aligned} \tag{19}$$

https://doi.org/10.1021/acsomega.2c05639
ACS Omega 2022, 7, 45189−45196

$$D_n = J_2'\left(\beta_{2n}\frac{\sigma}{2R}\right)\left[\frac{1}{4R}G_{2,4}^{2,1}\left(\beta_{2n}, \frac{1}{2}\middle|\begin{matrix}3/2,-3/2\\ 1,1,-\frac{3}{2,1}/2\end{matrix}\right) - \frac{1}{2a}G_{2,4}^{2,1}\left(\beta_{2n}\frac{\sigma}{2R}, \frac{1}{2}\middle|\begin{matrix}3/2,-3/2\\ 1,1,-\frac{3}{2,1}/2\end{matrix}\right)\right] - Y_2'\left(\beta_{2n}\frac{\sigma}{2R}\right)\left[\frac{1}{8}\frac{\beta_{2n}^2}{2R}{}_1F_2\left(\frac{1}{2}; \frac{3}{2}, 3; -\frac{\beta_{2n}^2}{4}\right) - \frac{\sigma\beta_{2n}^2}{32R^2}{}_1F_2\left(\frac{1}{2}; \frac{3}{2}, 3; -\frac{\sigma^2\beta_{2n}^2}{16R^2}\right)\right] \quad (20)$$

where ${}_1F_2(a_1; b_1, b_2; x)$ is the generalized hypergeometric function and $G_{2,4}^{2,1}\left(x, y\middle|\begin{matrix}a_1, a_2\\ b_1, b_2, b_3, b_4\end{matrix}\right)$ is the Meijer G-function.[59]

Substitution of eqs 15 and 16 into eq 3 leads to

$$J^{(0)}(0) = 4\pi N\sum_{n=1}^{\infty}\frac{\tau C_n^2}{\beta_{0n}^2 V_{0n}} \quad (21)$$

$$J^{(2)}(2\omega_0) = 4\pi N\sum_{n=1}^{\infty}\frac{D_n^2}{V_{2n}}\frac{\beta_{2n}^2\tau}{\beta_{2n}^4 + 4\omega_0^2\tau^2} \quad (22)$$

Inserting eqs 21 and 22 into eq 2, we obtained the dipolar cross-relaxation rate between nanoconfined fluids and the solid surface

$$R_{cr} = \frac{\mu_0^2\hbar^2\gamma^4 N\tau}{4\pi}\left(6\sum_{n=1}^{\infty}\frac{D_n^2}{V_{2n}}\frac{\beta_{2n}^2\tau}{\beta_{2n}^4 + 4\omega_0^2\tau^2} - \sum_{n=1}^{\infty}\frac{\tau C_n^2}{\beta_{0n}^2 V_{0n}}\right) \quad (23)$$

We evaluated eq 23 using Wolfram Mathematica 11.1 and plotted the cross-relaxation rate versus the closest distance of the fluid spin and spin on the pore surface σ in Figure 5. The

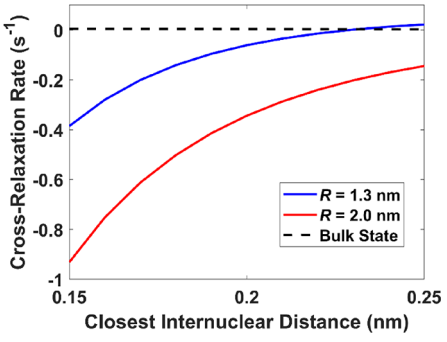

Figure 5. Cross-relaxation rate by varying the closest internuclear distance.

other parameters used were $N = 6.05 \times 10^{18}$ spins/m^2 for 2D number density; $D = 1.21 \times 10^{-9}$ m^2/s for the 2D diffusion coefficient which is 2/3 of the measured 3D diffusion coefficient (Figure S5 in the SI); and $\omega_0 = 500$ MHz. The dashed line in Figure 5 is for the bulk state calculated using eq 1 with 3D number density $N_A = 1.49 \times 10^{28}$ spin/m^3.

Using the pore radius of 1.3 nm from Figure 5 and the measured dipolar cross-relaxation rate -0.10 s^{-1} between methanol and MCM41-C1 matrix protons, we can estimate the closest approach of the fluid proton spin to the solid surface spin is approximately 0.19 nm. This is much larger than two times the hydrogen-atom radius of 0.12 nm. However, the relaxation theory derived here was based on uniform density and molecular dynamics of fluid in a perfectly spherical pore. All these conditions are only approximately true. Therefore, the difference could be due to these uncertainties.

The measured cross-relaxation rate between nanoconfined methanol protons and matrix solid protons is approximately $R_{cr} = -0.1$ s^{-1}, in contrast to the positive rate with a magnitude of 10^{-3} s^{-1} in bulk fluid. In the bulk state, negative NOE rates occur only for large, slowly diffusing molecules.[54] In deriving the dipolar cross-relaxation between nanoconfined fluid and solid, we used the same 2D diffusion coefficient for the fluid in nanopores on the time scale of $t \leq R^2/4D$ as in the bulk state, i.e., the molecule is free-tumbling in the pore. When the time scale is larger than $R^2/4D$, the molecules are reflected back into the pore by the pore wall, which would result in a much smaller macroscopic diffusion coefficient for the confined liquid than that in bulk liquid. The theoretical result based on this model is consistent with the measured cross-relaxation rate in both magnitude and sign, indicating that the free molecular tumbling in the nanopore in the time scale $t \leq R^2/4D$ is appropriate. It also indicates the nanoconfinement indeed enhances the dipolar cross-relaxation interaction of the fluids and matrix solid. Furthermore, in the calculation, we treated the fluid in the pore as continuous, so that eq 5 is valid. The average pore radius of MCM41-C1 is 1.3 nm, which only allows about 3 methanol molecules across the radius. This is approaching the limit in which a fluid can still be treated as continuous. For smaller pores, outside the continuous regime, the use of molecular dynamics simulations is needed to calculate the cross-relaxation rate between the fluid and the solid.

NMR relaxation is the result of time-modulated interactions with a time average of zero over the NMR measurement.[22,54] Thus, the upper limit of correlation time t in eq 4 must be several orders of magnitude smaller than the minimum NMR experimental time, typically 10^{-3} s. Therefore, the characteristic time constant τ defined in eq 24 needs to be shorter than 10^{-7} s. This τ limit then sets a limit on the application of the current theory for the fluid in pores with a given diffusion coefficient. As a result, the theory presented here may not work when $R > \sqrt{4D\tau} \approx 28$ nm for contained fluids with a diffusion coefficient of $D = 2 \times 10^{-9}$ m^2/s.

For the sample used in our experiment, the solid hydrogens in MCM41-C1 are only on the surface of the nanopore. Therefore, the hydrogen dipolar cross-relaxation is between this thin layer of solid and the entire pore fluid. However, in terms of dipolar relaxation between nanoconfined liquid and the matrix solid, a sample with hydrogen in the entire solid matrix is not very different from the sample used in this study because spin-diffusion between hydrogens in the solid state can rapidly equilibrate spin polarization among all solid hydrogens.[54] In addition, the observed enhancement of dipolar cross-relaxation between nanoconfined fluids and matrix solids is true for any pore shapes, although pores in MCM41-C1 is largely spherical, which allows easier theoretical calculation.

https://doi.org/10.1021/acsomega.2c05639
ACS Omega 2022, 7, 45189−45196

CONCLUSIONS

NMR dipolar cross-relaxation was used to investigate the interaction of nanoconfined fluids with matrix solids. Confining a fluid in a nanopore affects the molecular diffusion of the fluid thereby altering the interaction with surface species. This confinement changes the correlation of the fluid spins within the matrix solids and significantly enhances the NMR cross-relaxation interaction of nanoconfined fluids with the matrix.

The enhanced cross-relaxation of nanoconfined fluid with the matrix solid allows easy and accurate measurements using 1D and/or 2D NMR experiments. This method thus provides a direct approach to quantify the fluid-matrix interaction and may be applied to investigate many different nanoporous systems such as energy storage and subsurface extraction from organic-rich shales,[8] energy harvesting,[33] nanomedicine,[34,35] membrane science,[36] DNA nanopore sequencing,[37] macromolecules with nanocavities,[38] and cell organelles containing nanostructures such as fluids in mitochondrial compartments.[39,40]

DATA AVAILABILITY

The data and simulation of 2D diffusion codes for this study are available from the corresponding author upon request.

ASSOCIATED CONTENT

Supporting Information

The Supporting Information is available free of charge at https://pubs.acs.org/doi/10.1021/acsomega.2c05639.

^{29}Si DPMAS spectrum of sample MCM41-C1; pore size distribution of MCM41-C1; illustration of the experimental setup for preparing nano-confined fluids in silica gel using capillary condensation; ^{1}D NMR pulse sequence for selective NOE measurement with theory of signal intensity in the selective NOE experiments; fit of the NMR pulsed-field-gradient stimulated echo (PFG-STE) data of the CH_3OD at 22 °C for diffusion coefficients; distributions of the probability function at three-time instances (PDF)

AUTHOR INFORMATION

Corresponding Author

Jin-Hong Chen − *Aramco Americas: Aramco Research Center-Houston, Houston, Texas 77084, United States;* orcid.org/0000-0003-0722-0244; Email: JinHong.Chen@aramcamericas.com

Authors

Chao Liu − *Aramco Americas: Aramco Research Center-Houston, Houston, Texas 77084, United States*

Stacey M Althaus − *Aramco Americas: Aramco Research Center-Houston, Houston, Texas 77084, United States;* orcid.org/0000-0002-3487-8001

Mohammed Boudjatit − *Saudi Aramco, Dhahran 31311, Saudi Arabia*

Complete contact information is available at: https://pubs.acs.org/10.1021/acsomega.2c05639

Notes

The authors declare no competing financial interest.

ACKNOWLEDGMENTS

We thank Wei Wang for measurement of pore size distribution in silica gels using nitrogen desorption and Qiushi Sun for helpful discussion.

REFERENCES

(1) Barrat, J.-L.; Bocquet, L. Large Slip Effect at a Nonwetting Fluid-Solid Interface. *Phys. Rev. Lett.* **1999**, *82*, 4671−4674.

(2) Xing, J. T.*In Fluid-Solid Interaction Dynamics*; Xing, J. T., Ed. Academic Press: 2019; pp. xi-xvi.

(3) Han, Y.; Cundall, P. A. LBM−DEM modeling of fluid−solid interaction in porous media. *INT. J. NUMER. ANAL. METHODS GEOMECH.* **2013**, *37*, 1391−1407.

(4) Nanofluidics is on the rise. *Nat. Mater.***2020**, *19* (), 253, DOI: 10.1038/s41563-020-0633-8.

(5) Wu, K.; Chen, Z.; Li, X.; Guo, C.; Wei, M. A model for multiple transport mechanisms through nanopores of shale gas reservoirs with real gas effect−adsorption-mechanic coupling. *Int. J. Heat Mass Transfer* **2016**, *93*, 408−426.

(6) Liu, C.; Li, F.; Ma, L.-P.; Cheng, H.-M. Advanced Materials for Energy Storage. *Adv. Mater.* **2010**, *22*, E28−E62.

(7) Chapman, N. A.; McKinley, I. G.; Hill, M. D., *The geological disposal of nuclear waste*. John Wiley and Sons: United Kingdom, 1987.

(8) Loucks, R. G.; Reed, R. M.; Ruppel, S. C.; Jarvie, D. M. Morphology, Genesis, and Distribution of Nanometer-Scale Pores in Siliceous Mudstones of the Mississippian Barnett Shale. *J. Sediment. Res.* **2009**, *79*, 848−861.

(9) Chen, J.-H.; Zhang, J.; Jin, G.; Quinn, T.; Frost, E.; Chen, J.*In Capillary Condensation And NMR Relaxation Time In Unconventional Shale Hydrocarbon Resources, SPWLA 53rd Annual Logging Symposium*, Cartagena, Colombia, Cartagena, Colombia, 2012.

(10) Tao, Z.; Clarens, A. Estimating the Carbon Sequestration Capacity of Shale Formations Using Methane Production Rates. *Environ. Sci. Technol.* **2013**, *47*, 11318−11325.

(11) Freire, E.; Mayorga, O. L.; Straume, M. Isothermal titration calorimetry. *Anal. Chem.* **1990**, *62*, 950A−959A.

(12) Bhat, T. N.; Bentley, G. A.; Boulot, G.; Greene, M. I.; Tello, D.; Dall'Acqua, W.; Souchon, H.; Schwarz, F. P.; Mariuzza, R. A.; Poljak, R. J. Bound water molecules and conformational stabilization help mediate an antigen-antibody association. *Proc. Natl. Acad. Sci. U. S. A.* **1994**, *91*, 1089−1093.

(13) Thommes, M.; Kaneko, K.; Neimark, A.; Olivier, J. P.; Rodriguez-Reinoso, F.; Rouquerol, J.; Sing, K. S. W. Physisorption of gases, with special reference to the evaluation of surface area and pore size distribution (IUPAC Technical Report). *Pure Appl. Chem.* **2015**, *87*, 1051−1069.

(14) Cychosz, K. A.; Guillet-Nicolas, R.; García-Martínez, J.; Thommes, M. Recent advances in the textural characterization of hierarchically structured nanoporous materials. *Chem. Soc. Rev.* **2017**, *46*, 389−414.

(15) Chiang, W.-S.; Fratini, E.; Baglioni, P.; Georgi, D.; Chen, J.-H.; Liu, Y. Methane Adsorption in Model Mesoporous Material, SBA-15, Studied by Small-Angle Neutron Scattering. *J. Phys. Chem. C* **2016**, *120*, 4354−4363.

(16) Luo, M.-F.; Fang, P.; He, M.; Xie, Y.-L. In situ XRD, Raman, and TPR studies of CuO/Al2O3 catalysts for CO oxidation. *J. Mol. Catal. A: Chem.* **2005**, *239*, 243−248.

(17) Hunter, R. J.; Ottewill, R. H.; Rowell, R. L., *Zeta Potential in Colloid Science: Principles and Applications*. Elsevier Science: 2013.

(18) Wang, X., *Fundamentals of Fluid-Solid Interactions: Analytical and Computational Approaches*. Elsevier Science: 2008.

(19) Slichter, C. P., *Principles of Magnetic Resonance*. Springer Science & Business Media: 1990.

(20) Bronnimann, C. E.; Zeigler, R. C.; Maciel, G. E. Proton NMR study of dehydration of the silica gel surface. *J. Am. Chem. Soc.* **1988**, *110*, 2023−2026.

(21) Maciel, G. E.; Haw, J. F.; Chuang, I. S.; Hawkins, B. L.; Early, T. A.; McKay, D. R.; Petrakis, L. NMR studies of pyridine on silica-alumina. *J. Am. Chem. Soc.* **1983**, *105*, 5529−5535.
(22) Bloembergen, N.; Purcell, E. M.; Pound, R. V. Relaxation Effects in Nuclear Magnetic Resonance Absorption. *Phys. Rev.* **1948**, *73*, 679−712.
(23) Wuthrich, K. Protein structure determination in solution by nuclear magnetic resonance spectroscopy. *Science* **1989**, *243*, 45−50.
(24) Faux, D. A.; McDonald, P. J. Nuclear-magnetic-resonance relaxation rates for fluid confined to closed, channel, or planar pores. *Phys. Rev. E* **2018**, *98*, 063110.
(25) Korb, J.-P. Nuclear magnetic relaxation of liquids in porous media. *New J. Phys.* **2011**, *13*, 035016.
(26) Brown, R. J. S.; Fatt, I.*In Measurements Of Fractional Wettability Of Oil Fields' Rocks By The Nuclear Magnetic Relaxation Method*, Fall Meeting of the Petroleum Branch of AIME, 1956.
(27) Kleinberg, R. L.; Kenyon, W. E.; Mitra, P. P. Mechanism of NMR Relaxation of Fluids in Rock. *J. Magn. Reson., Ser. A* **1994**, *108*, 206−214.
(28) Kenyon, W. E.Petrophysical Principles of Applications of NMR Logging. *SPWLA-1991-v32n5a5***1997**, *38* ().
(29) Foley, I.; Farooqui, S. A.; Kleinberg, R. L. Effect of Paramagnetic Ions on NMR Relaxation of Fluids at Solid Surfaces. *J. Magn. Reson., Ser. A* **1996**, *123*, 95−104.
(30) Andrew, E. R.; Bradbury, A.; Eades, R. G. Nuclear Magnetic Resonance Spectra from a Crystal rotated at High Speed. *Nature* **1958**, *182*, 1659−1659.
(31) Chen, J.-H.; Singer, S., High-Resolution Magic Angle Spinning NMR Spectroscopy. In *The Handbook of Metabonomics and Metabolomics*, Lindon, J. C.; Nicholson, J. K.; Holmes, E., Eds. Elsevier Science B.V.: Amsterdam, 2007; pp. 113−147.
(32) Chen, J.-H.; Haghmoradi, A.; Althaus, S. M. NMR Intermolecular Dipolar Cross-Relaxation in Nanoconfined Fluids. *J. Phys. Chem. B* **2020**, *124*, 10237−10244.
(33) Siria, A.; Poncharal, P.; Biance, A.-L.; Fulcrand, R.; Blase, X.; Purcell, S. T.; Bocquet, L. Giant osmotic energy conversion measured in a single transmembrane boron nitride nanotube. *Nature* **2013**, *494*, 455−458.
(34) Sun, C.; Lee, J. S. H.; Zhang, M. Magnetic nanoparticles in MR imaging and drug delivery. *Adv. Drug Delivery Rev.* **2008**, *60*, 1252−1265.
(35) Allen, T. M.; Cullis, P. R. Drug Delivery Systems: Entering the Mainstream. *Science* **2004**, *303*, 1818−1822.
(36) Tu, Y.-M.; Song, W.; Ren, T.; Shen, Y. X.; Chowdhury, R.; Rajapaksha, P.; Culp, T. E.; Samineni, L.; Lang, C.; Thokkadam, A.; Carson, D.; Dai, Y.; Mukthar, A.; Zhang, M.; Parshin, A.; Sloand, J. N.; Medina, S. H.; Grzelakowski, M.; Bhattacharya, D.; Phillip, W. A.; Gomez, E. D.; Hickey, R. J.; Wei, Y.; Kumar, M. Rapid fabrication of precise high-throughput filters from membrane protein nanosheets. *Nat. Mater.* **2020**, *19*, 347−354.
(37) Branton, D.; Deamer, D. W.; Marziali, A.; Bayley, H.; Benner, S. A.; Butler, T.; Di Ventra, M.; Garaj, S.; Hibbs, A.; Huang, X.; Jovanovich, S. B.; Krstic, P. S.; Lindsay, S.; Ling, X. S.; Mastrangelo, C. H.; Meller, A.; Oliver, J. S.; Pershin, Y. V.; Ramsey, J. M.; Riehn, R.; Soni, G. V.; Tabard-Cossa, V.; Wanunu, M.; Wiggin, M.; Schloss, J. A. The potential and challenges of nanopore sequencing. *Nat. Biotechnol.* **2008**, *26*, 1146−1153.
(38) Ernst, J. A.; Clubb, R. T.; Zhou, H.-X.; Gronenborn, A. M.; Clore, G. M. Response: Use of NMR to Detect Water Within Nonpolar Protein Cavities. *Science* **1995**, *270*, 1848−1849.
(39) Logan, D. C. The mitochondrial compartment. *J. Exp. Bot.* **2006**, *57*, 1225−1243.
(40) Lefkimmiatis, K.; Leronni, D.; Hofer, A. M. The inner and outer compartments of mitochondria are sites of distinct cAMP/PKA signaling dynamics. *J. Cell Biol.* **2013**, *202*, 453−462.
(41) Barrett, E. P.; Joyner, L. G.; Halenda, P. P. The Determination of Pore Volume and Area Distributions in Porous Substances. I. Computations from Nitrogen Isotherms. *J. Am. Chem. Soc.* **1951**, *73*, 373−380.
(42) Thomson, W. L. K. On the equilibrium of vapor at a curved surface of liquids. *Philos. Mag.* **1871**, *42*, 448−452.
(43) Barsotti, E.; Tan, S. P.; Saraji, S.; Piri, M.; Chen, J.-H. A review on capillary condensation in nanoporous media: Implications for hydrocarbon recovery from tight reservoirs. *Fuel* **2016**, *184*, 344−361.
(44) Lowe, I. J. Free Induction Decays of Rotating Solids. *Phys. Rev. Lett.* **1959**, *2*, 285−287.
(45) Chen, J.; Singer, S., *High-Resolution Magic Angle Spinning NMR Spectroscopy*. 2007; pp. 113−147.
(46) Vold, R. L.; Waugh, J. S.; Klein, M. P.; Phelps, D. E. Measurement of Spin Relaxation in Complex Systems. *J. Chem. Phys.* **1968**, *48*, 3831−3832.
(47) Jeener, J.; Meier, B. H.; Bachmann, P.; Ernst, R. R. Investigation of exchange processes by two-dimensional NMR spectroscopy. *J. Chem. Phys.* **1979**, *71*, 4546−4553.
(48) Macura, S.; Ernst, R. R. Elucidation of cross relaxation in liquids by two-dimensional N.M.R. spectroscopy. *Mol. Phys.* **1980**, *41*, 95−117.
(49) Geen, H.; Freeman, R. Band-selective radiofrequency pulses. *J. Magn. Reson.* **1991**, *93*, 93−141.
(50) Kresge, C. T.; Leonowicz, M. E.; Roth, W. J.; Vartuli, J. C.; Beck, J. S. Ordered mesoporous molecular sieves synthesized by a liquid-crystal template mechanism. *Nature* **1992**, *359*, 710−712.
(51) Kessler, H.; Oschkinat, H.; Griesinger, C.; Bermel, W. Transformation of homonuclear two-dimensional NMR techniques into one-dimensional techniques using Gaussian pulses. *J. Magn. Reson.* **1986**, *70*, 106−133.
(52) Chen, J.-H.; Sambol, E. B.; DeCarolis, P.; O'Connor, R.; Geha, R. C.; Wu, Y. V.; Singer, S. High-resolution MAS NMR spectroscopy detection of the spin magnetization exchange by cross-relaxation and chemical exchange in intact cell lines and human tissue specimens. *Magn. Reson. Med.* **2006**, *55*, 1246−1256.
(53) Avinadav, C.*Multiple curve fitting with common parameters using NLINFIT*, MATLAB Central File Exchange, 2016.
(54) Abragam, A., *The Principles of Nuclear Magnetism*. Clarendon Press: London, 1961.
(55) Torrey, H. C. Nuclear Spin Relaxation by Translational Diffusion. *Phys. Rev.* **1953**, *92*, 962−969.
(56) Noggle, J. H.; Schirmer, R. E., *The Nuclear Overhauser Effect*.Chemical Applications. Academic Press: New York, 1971.
(57) Faux, D. A.; McDonald, P. J.; Howlett, N. C.; Bhatt, J. S.; Churakov, S. V. Nuclear magnetic resonance relaxometry of water in two and quasi-two dimensions. *Phys. Rev. E* **2013**, *87*, 062309.
(58) Ölçer, N. Y.; Sunderland, J. E. Unsteady heat conduction in finite hollow circular cylinders under time-dependent boundary conditions of the second kind. *Nucl. Eng. Des.* **1968**, *8*, 201−223.
(59) Weisstein, E. W.*From MathWorld--A Wolfram Web Resource*.

https://doi.org/10.1021/acsomega.2c05639
ACS Omega 2022, 7, 45189−45196